NJC

New Journal of Chemistry

A journal for new directions in chemistry

Accepted Manuscript

This article can be cited before page numbers have been issued, to do this please use: V. Luxami, G. Kumar, S. Chopra and I. Singh, *New J. Chem.*, 2026, DOI: 10.1039/D5NJ03370E.

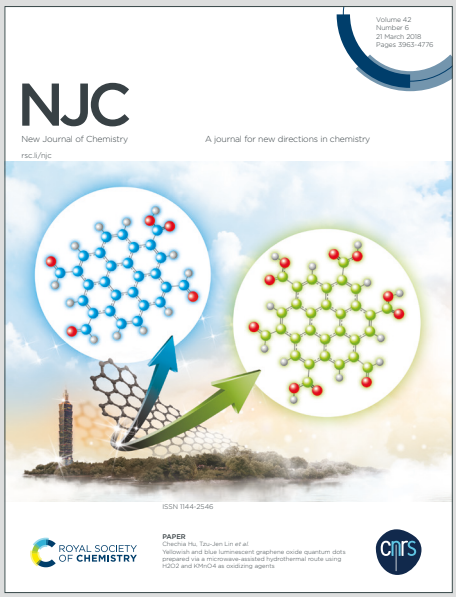

ROYAL SOCIETY OF CHEMISTRY

rsc.li/njc

Title: Naphthalimide- benzimidazole conjugate for the light-up fluorescence detection of Ga^{3+} and DCP

Shifali Chopra[a], Gulshan Kumar[b], Iqubal Singh[c] and Vijay Luxami[a*]

[a] Department of Chemistry and Biochemistry, Thapar Institute of Engineering and Technology, Patiala-147001, India

[b] Department of Chemistry, Banasthali University, Banasthali Newai 304022, Rajasthan, India

[c] School of Pharmaceutical Sciences, Lovely Professional University, Phagwara 144411, India

[a*]Email: vluxami@thapar.edu

Abstract

Gallium ions (Ga^{3+}) play a crucial role in human life due to their remarkable physical, chemical, and biological properties, with applications ranging from electronic devices and solar cells to anticancer therapeutics, owing to their strong affinity for tumor tissues. However, increasing industrial and biomedical use has led to environmental accumulation, making Ga^{3+} exposure a concern. In this work, we report a novel naphthalimide-based reversible chelating ligand (**NaHB**) capable of selectively recognizing both Ga^{3+} ions and the nerve agent diethyl chlorophosphate (DCP) in a CH_3CN/H_2O medium. The binding interactions were systematically studied using UV–Vis absorption, fluorescence spectroscopy, NMR, and high-resolution mass spectrometry. **NaHB** displays an instantaneous "switch-on" fluorescence response toward Ga^{3+} and DCP, with binding constants (K_a) of 5.15×10^4 M^{-1} and 1.2×10^5 M^{-1}, respectively. Job's plot analysis confirmed a 1:1 stoichiometry for both systems. The practical utility of **NaHB** was demonstrated through paper strip assays and quantitative detection of Ga^{3+} and DCP in real-field water samples. Furthermore, the **NaHB**–Ga^{3+} complex was explored for molecular logic gate applications, showcasing its multifunctional sensing capability.

Keywords: Naphthalimide-benzidazole; Ga^{3+} and DCP chemosensor; 'Turn-on' fluorescence; Paper strip; Logic gate; Real-time monitoring

1. Introduction

Over the past few decades, chemosensors have gained much interest in sensing of ions and molecules which are playing crucial role in the environment [1–7]. Gallium is a rare element

found in trace amount as salts in various ores and soil, but it has an imperative impact on humans lives [8–10]. The manufacturing of integrated circuits, semiconductor devices, and optoelectronic components including light-emitting diodes, solar cells, and photodetectors heavily relies on the utilization of gallium salts [11–14]. Gallium compounds are employed clinically as markers for diagnosis and therapeutic agents because of their capacity to target tumors. Ga^{3+} ions also have a great affinity for tumors, and their nitrate salts have long been used as antitumor agents. The presence of these substances' residues in the body or environment is dangerous. Its usage as a chemotherapy treatment agent, is a sign of its possible cell-damaging effects. Ga^{3+} exposure in occupational contexts and from pollution in the environment can have adverse effects on the kidneys, the immunological system, the heart, and the testicles [15–17]. As a result, the requirement for identifying the presence of Ga^{3+} has increased and sparked academic curiosity, not only because of its function as a pollutant but it can also be used to track cancer treatments and monitor tumors [18–20]. For both health and financial reasons, it is urgently necessary to develop precise and effective technology to detect traces of gallium.

On the other hand, Chemical Warfare Nerve Agents (CWNAs) are a class of OPs (Organophosphates) with a phosphate or phosphite group that is extremely poisonous. Even a trace amount of inhalation can cause deaths in a short time [21,22]. OPs are generally utilized as pesticides and herbicides in agriculture because these have chemically reactive phosphate ester side chains [23]. Sarin (GB), soman (GD), and tabun (GA) are found to be three extremely lethal organophosphate nerve agents. These compounds' reactive phosphate groups can interact with hydroxyl groups of acetylcholinesterase (AChE) enzyme. Acetylcholine (ACh), a neurotransmitter found in postsynaptic membranes and neuromuscular junctions, hydrolysed by AChE. Acetylcholine breakdown is blocked, causing a neurological imbalance that swiftly results in organ failure, dysfunction of the central nervous system, and death [21,24-26]. Diethyl chlorophosphate (DCP), a related substance, is frequently utilized to simulate sarin for scientific studies. Comparing DCP to real nerve agents reveals that it has a similar level of responsiveness but is somewhat less hazardous [27,28]. Moreover, organo-phosphates are routinely employed in agriculture to control pests despite being harmful to human health [29]. These need to be closely watched because there is a considerable likelihood that they will accumulate within the food system as a result of agricultural usage. As a result, an organophosphate contaminant found in consuming goods appears to be extremely dangerous to human health. Due to their lack of colour, flavour, and smell, these chemicals are difficult to identify [30].

View Article Online
DOI: 10.1039/D5NJ03370E

Research groups have already developed methodology based on colorimetry, fluorometry, and enzymatic assays to identify organophosphates [31–34]. Because of the selectivity, sensitivity, quick reaction, and on-site analysis, fluorometric approaches have gained more attention. Herein, we report the synthesis of a fluorescent probe (NaHB) incorporating a naphthalimide core conjugated with a benzimidazole unit, featuring a donor hydroxyl (–OH) group and an acceptor nitrogen atom of the benzimidazole. The system undergoes excited-state intramolecular proton transfer (ESIPT), in which the proton from the hydroxyl group in the ground-state enol form is transferred to the benzimidazole nitrogen in the excited state, generating the keto tautomer. This tautomerization process is stabilized by intramolecular hydrogen bonding, enabling distinct photophysical properties. On complexation of **NaHB**+Ga^{3+} and also the phosphorylation of **NaHB** in the presence of DCP, restricted the ESIPT process resulting in significant enhancement of the fluorescence signal. Hence, probe has been designed exhibiting high sensitivity and superfast response towards Ga^{3+} and DCP in liquid state followed by quantification in real field water samples.

The **NaHB** chemosensor was rationally designed by fusing two photofunctional units—naphthalimide and benzimidazole—to harness the synergistic effects of intramolecular charge transfer (ICT) and excited-state intramolecular proton transfer (ESIPT) within a single molecular framework. The naphthalimide moiety serves as a robust, π-conjugated fluorophore with strong absorption in the visible region and high photostability, acting as an electron acceptor. The benzimidazole unit, on the other hand, introduces electron-donating nitrogen sites and a proton-active –NH group, which collectively enable both metal coordination and ESIPT behaviour. This hybrid structure allows the probe to interact with analytes through two orthogonal mechanisms: (i) chelation with Ga^{3+} ions, where coordination to the nitrogen and carbonyl oxygen atoms suppresses non-radiative PET/ESIPT processes, leading to a chelation-enhanced fluorescence (CHEF) response; and (ii) electrophilic interaction with DCP, in which the phosphorylation at the –OH site perturbs the ESIPT equilibrium, producing a distinct emission modulation. The deliberate fusion of these two responsive motifs within the NaHB framework thus enables selective and differential optical responses toward Ga^{3+} and DCP, establishing a rational molecular design concept for future multifunctional sensing systems.

2. Experimental section

2.1 Materials and methods

Chemicals used for synthesis were purchased from Loba Chemie, Sigma-Aldrich, and Spectrochem depending upon their availability. Spectroscopic grade solvents were purchased from Spectrochem and Rankem Ltd. and were used without any further purification. Reaction progress was monitored with the help of TLC (Thin Layer Chromatography).

2.2 Synthesis of 3-bromo-7*H*-benzo[*de*]benzo[4,5]imidazo[2,1-*a*]isoquinolin-7-one (Compound 3)

Compounds **1** and **2** were synthesized in accordance with the previously reported literature methods [35,36]. For the synthesis of compound **3**, compound **1** (200 mg, 0.575 mmol) and compound **2** (143 mg, 0.575 mmol) were dissolved in CH_3CN: H_2O (9:1) (10 ml) in the presence of K_2CO_3 (100 mg, 0.724 mmol) and $Pd(PPh_3)_4$ (6 mg, 0.005 mmol) in Suzuki-Miyaura cross coupling reaction **(Scheme 1)**. The reaction mixture was refluxed for 8 h until the starting materials were completely consumed, which was monitored through TLC. After completion, the reaction mixture was cooled to room temperature. The excess solvent was evaporated, followed by the addition of 50 ml of cold water. The precipitates formed were filtered to obtain a crude product which was purified by column chromatography using $CHCl_3$: EtOAc (80:20) as eluent to afford the pure yellow colored product **3** in 85% yield. M.pt. >300 ℃. ^{1}H NMR of compound **3** ($CDCl_3$, 400 MHz): □ (ppm) 11.2 (d, J = 7.36 Hz, 1H, OH), 10.01 (s, 1H, CHO), 8.89 (d, J = 6.4 Hz, 1H, ArH), 8.83 (m, 1H, ArH), 8.57 (m,1H, ArH), 8.14 (d, J = 8.48 Hz, 1H, ArH), 7.89 (t, 1H, ArH), 7.75 (m, 4H, ArH), 7.50 (m, 2H, ArH), 7.20 (m, 1H, ArH) **(Figure S1)**. ^{13}C NMR of compound **3** ($CDCl_3$, 100 MHz): □ (ppm) 196.5, 191.8, 161.9, 145.6, 145.2, 135.8, 135.3, 132.3, 131.7, 130.5, 130.4, 128.1, 127.1, 120.8, 118.6 **(Figure S2)**. HRMS (ESI-TOF): (m/z) $[M + H]^+$ calcd for $C_{25}H_{15}N_2O_3$: 391.1004, found: 391.1010.

2.3 Synthesis of 3-(3-(1*H*-benzo[*d*]imidazol-2-yl)-4-hydroxyphenyl)-7*H*-benzo[*de*]benzo[4,5]imidazo[2,1-*a*]isoquinolin-7-one (NaHB)

To a stirred solution of compound **3** (200 mg, 0.512 mmol) in nitrobenzene (5 ml), *o*-phenylenediamine (60 mg, 0.55 mmol) was added and the reaction mixture was heated to 80 ℃ for 6 h. After completion of reaction, monitored by TLC, hexane (30 ml) was added to the reaction mixture, and the solid product was separated which was then filtered off and washed with hexane and diethyl ether. After vacuum drying, the pure yellow solid of **NaHB** was obtained in 80% yield. M.pt. >300 ℃. ^{1}H NMR of **NaHB** ($CDCl_3$, 400 MHz): □ (ppm) 8.25 (m, 2H, ArH), 7.93 (m, 2H, ArH), 7.78 (m, 1H, ArH), 7.33 (m, 3H, ArH), 7.04 (m, 2H, ArH), 6.93 (m, 2H, ArH), 6.70 (m, 4H, ArH). ^{13}C NMR of **NaHB** ($CDCl_3$, 100 MHz): □ (ppm) 200.5,

View Article Online
DOI: 10.1039/D5NJ03370E

191.7, 191.5, 163.4, 145.4, 142.6, 138.4, 135.8, 135.2, 131.8, 130.8, 130.5, 129.8, 129.6, 127.1, 119.6, 119.0. HRMS (ESI-TOF): (m/z) $[M + H]^+$ calcd for $C_{31}H_{19}N_4O_2$: 479.1508, found: 479.1506. **(Figure S3-S5).**

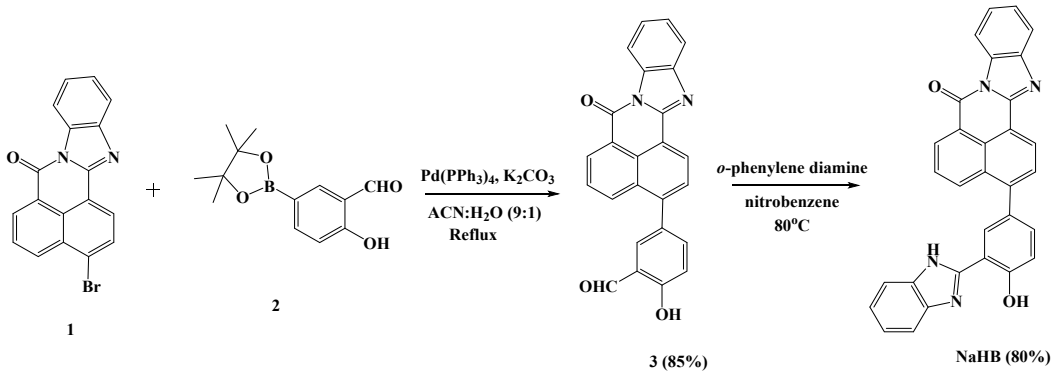

Scheme 1: Synthetic route for **NaHB**

2.4 Instruments

^1H NMR and ^{13}C NMR spectra were recorded on JEOL ECS-400 MHz spectrometer at ambient temperature in $CDCl_3$ with TMS as an internal reference. All chemical shifts were reported in ppm with respect to the reference. The mass spectra of the synthesized compounds were recorded using XEVO G2-XS QTOF of Waters. The absorption spectra were recorded on SHIMADZU-2600 spectrophotometer and quartz cuvettes of 1 cm in path length. The fluorescence spectra were recorded on a Varian Carey Eclipse fluorescence spectrophotometer using a slit width (excitation = 20 nm, emission = 20 nm) at stated excitation. The lifetime decay studies were executed on DeltaFlex Modular Fluorescence Life-time Spectrofluorimeter (HORIBA Scientific).

2.5 Spectroscopic studies

The photophysical properties of **NaHB** were studied by preparing a stock solution of 1 mM using dimethyl sulfoxide. UV-Visible and fluorescence studies with various metal ions (Na^+, K^+, Mg^{2+}, Al^{3+}, Ca^{2+}, Fe^{2+}, Fe^{3+}, Co^{2+}, Ni^{2+}, Cu^{2+}, Zn^{2+}, Ga^{3+}, Cd^{2+}, Ba^{2+}, Hg^{2+} and Pb^{2+}) as their perchlorate salts and anions (CH_3COO^-, F^-, Cl^-, Br^-, CN^-, $H_2PO_4^-$, HSO_4^-, NO_3^-, AcO^-, ClO^-, $P_2O_7^{4-}$, SCN^- as tetra butyl ammonium salts (concentration = 10^{-1} M) and nerve agents DCP (Diethyl chloro phosphate), TEP (Triethyl phosphate), *N*-BP (*N*-Butyl phosphate)), were performed in CH_3CN: H_2O (9:1) to illustrate the ion sensing behaviour of **NaHB**. The stoichiometry of the complex was determined by Job's plot. Further titration studies were done to determine the detection limit and the binding constant values of the complex formed.

View Article Online
DOI: 10.1039/D5NJ03370E

2.6 Determination of detection limit

The limit of detection (LOD) was calculated based on the fluorescence titrations. To determine the S/N ratio, the emission intensity of the **NaHB** (10 μM) was performed in triplicate (n = 3). Standard deviations (SD) were calculated from replicate data, and 95% confidence intervals were determined using Student's t-distribution. The detection limit was then calculated using the equation (1).

$$\text{Detection limit (LOD)} = 3\sigma/k \quad \text{.....(1)}$$

where σ is the standard deviation of blank measurements; k is the slope of intensity versus sample concentration calibration curve. Stability constants were determined using Benesi-Hildebrand equation (2).

$$\frac{1}{I-I_0} = \frac{1}{K_a[I_{max}\text{-}I_0][C]^n} + \frac{1}{[I_{max}\text{-}I_0]} \quad \text{.....(2)}$$

Where I_o, I, and I_{max} are the absorption/emission intensities of the ligand in the absence of an analyte, at an intermediate analyte concentration, and a concentration of complete interaction with an analyte, respectively. K_a is the binding constant, C is the concentration of analyte, and n is the number of analytes bound per molecule.

2.7 Computational study

Geometry optimization of **NaHB** at the ground state (S_o) was carried out using density functional theory (DFT) at B3LYP/6-311g(d) level [37]. The solvation effect of acetonitrile was used to accompany the experimental environment and was estimated using the IEFPCM model. The stability of molecular structures was confirmed with no imaginary vibration frequencies. Further, the Time-Dependent DFT (TDDFT) method was used to calculate the excitation energies. The structural optimization and excitation energies calculation were also carried out at different basis sets at the same level of functional theory (6-311g(d); and 6-311g(d,p)); where outcomes of B3lyp/6-311g(d) were near to observed results. Thus, for all subsequent calculations, including geometry optimization, potential energy curves (PECs) for the proton transfer at S_o, and the first excited state (S_1), we use B3lyp/6-311g(d). All DFT and TDDFT calculations were carried out using Gaussian 16 [38].

2.8 Paper strip fabrication

View Article Online
DOI: 10.1039/D5NJ03370E

The strips were prepared by immersing Whatman filter paper (grade 1) in a stock solution of the probe **NaHB** (1×10^{-3} M) for 5 min, then it was air-dried, and stored in dark, airtight conditions at room temperature. The resulting changes in the colour, by dropwise addition of ions, were observed under 365 nm UV light allowing the detection of Ga^{3+} and DCP. The strips retained over 90% of their fluorescence intensity after 15 days, confirming good stability.

3. Results and discussion

3.1 Photophysical studies

Photophysical characteristics of **NaHB** were investigated using absorption and emission spectroscopic techniques. The absorption maximum for **NaHB** (10 μM, CH_3CN: H_2O (1:9; v/v)) was observed at 402 nm. The **NaHB** on excitation at 402 nm showed emission at 520 nm with Stokes shift of 118 nm **(Figure 1)**. In order to study the effect of solvents, absorption and emission spectra of **NaHB** were examined in a variety of solvents **(Table 1)**. While the solvent polarity was increased, a redshift of 25 nm from 398 nm (cyclohexane) to 423 nm (water) was found in the case of absorption spectra **(Figure 2(a))**. Also, the **NaHB** extended its emission maxima region from 510 nm (cyclohexane) to 630 nm (water) as the solvent's polarity increased **(Figure 2(b))**. This amply demonstrates that on increasing polarity, the excited state becomes more stabilized. The charge transfer could be a possible reason for the expansion of emission spectra in polar solvents. The noticeably emission colour change with solvent polarity was observed, in line with spectral shifts **(Figure 2(c))**.

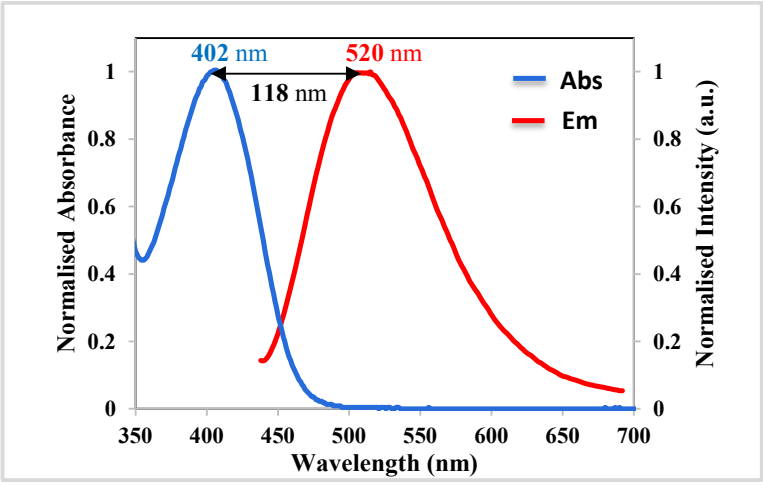

Figure 1. Normalized absorption and emission spectra of **NaHB** (10 μM, CH_3CN: H_2O (9:1); λ_{ex} = 402 nm)

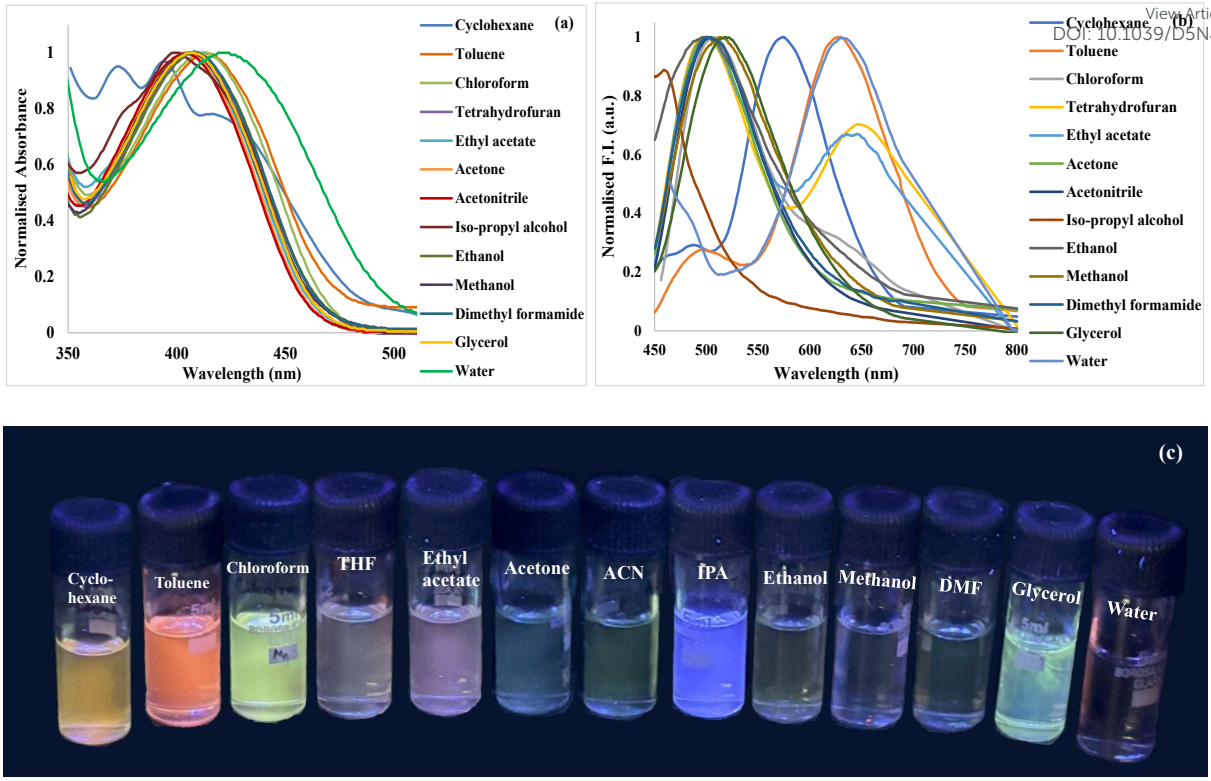

Figure 2. (a) Normalized absorption spectra, **(b)** Normalised emission spectra of **NaHB** (10 μM) in different solvents and **(c)** Effect of different solvents of **NaHB** under UV light

Table 1. Photophysical behaviour of **NaHB** (10 μM) in solvents of different polarity

Solvent	**λ_{max} (nm) (abs)**	**Molar absorptivity constant $\varepsilon = M^{-1}cm^{-1}$**	**λ_{em} (nm)**	**Stokes shift $\Delta\nu$ (cm^{-1})**	**Quantum Yield (ϕ)**
Cyclohexane	394	5100	481	4590	0.13
Toluene	410	24,000	560	6530	0.017
$CHCl_3$	415	21,100	505	4290	0.014
THF	407	22,600	501	4610	0.36
IPA	401	25,200	461	3245	0.05
Acetone	409	23,200	501	4490	0.27
Ethanol	407	23,200	500	4570	0.10
Methanol	406	23,400	516	5250	0.12
DMF	407	22,100	501	4610	0.11
CH_3CN	406	23800	502	4710	0.08
DMSO	390	23,300	460	3900	0.12
Glycerol	409	22,500	455	2470	0.28
H_2O	425	13600	631	7681	0.14

3.2. Ground state optimization and electronic charge distribution

View Article Online
DOI: 10.1039/D5NJ03370E

We optimized **NaHB** using the B3LYP/6-311G(d) method and calculated three nearby excitations to get an insight into the nature of the absorption spectra. The S_0-S_1 was calculated from transitions contribution of 98.4% involving the highest occupied molecular orbital (HOMO) to the lowest unoccupied molecular orbital (LUMO) at 437 nm with an oscillation strength of 0.6081. Further, S_0-S_2 and S_0-S_3 were calculated at 399 nm (HOMO-1→LUMO (97 %); f = 0.0904), and 358 nm (HOMO-4→LUMO (72 %); f = 0.033), respectively. Among these transitions, S_0-S_1 has the highest oscillation strength and is therefore considered for further discussion. HOMO→LUMO transition shows electron density shift from benzimidazole unit to naphthalimide unit indicating intramolecular charge transfer. Further, the nature of electronic also understood by natural transition orbitals, which also depicted that HOMO was evenly distributed over the whole architecture, while the LUMO was distributed over naphthalimide region only (**Figure S6**). Further, hole-electron distribution and intramolecular fragment charge transfer were calculated using Multiwfn [39-41]. It was inferred that electronic transition was occurred with low electron-hole overlap (Sr = 0.53092) and a charge separation of 4.3 Å (**Figure 3**). Moreover, the intramolecular fragment charge transferred from benzimidazole and fused phenylenediamine unit towards naphthalimide unit by 0.52872 and 0.08759 a.u., respectively with intrinsic charge transfer character of 72 %. These results showed that the electronic transition has intramolecular charge transfer nature.

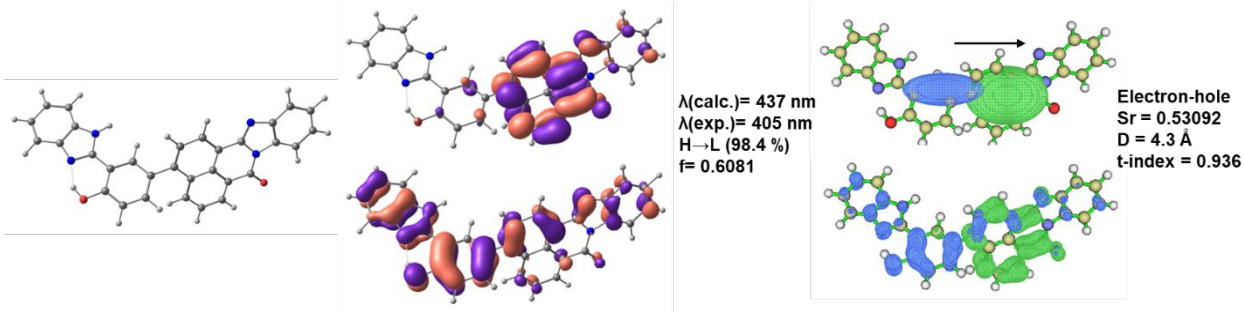

Figure 3. Optimized structures of **NaHB** and contributing molecular orbitals along with electron-hole distribution for $S_0 \rightarrow S_1$ transition

3.3. Intramolecular proton transfer or charge transfer

Because **NaHB** contains an acidic phenolic unit and a basic benzimidazole unit, which interact through small distances and could result in proton transfer at excited state. Further, we established the necessary condition of intramolecular hydrogen bonding strengthening at the S_0 and S_1 states to understand the **NaHB**'s behaviour towards ESIPT process. At S_0 state, the $O_{28}H_{50}\cdots N_{30}$ interaction has a distance of 1.728 Å and an interaction angle of 146.72º, which on photoexcitation at S_1 state, the interaction distance decreased to 1.690 Å and interaction

View Article Online
DOI: 10.1039/D5NJ03370E

angle increased to 146.84º **(Figure 4(a))**. Further, $O_{34}H_{35}\cdots N_{22}$ IraHB (Intramolecular Hydrogen Bonding) exhibited a 179 cm^{-1} redshift from 3178 cm^{-1} to 2999 cm^{-1} on photoexcitation to S_1 state **Figure 4(b)**. It was also noteworthy that **NaHB** approaches the molecular planarity by decreasing the dihedral angle between benzimidazole unit and naphthalimide unit from 53.68º to 43.54º at the S_1 state.

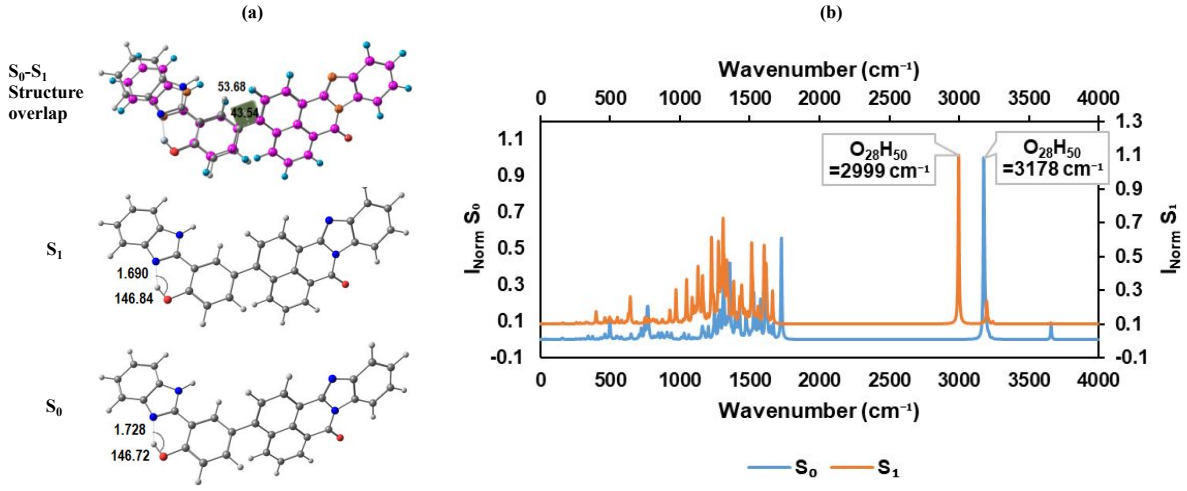

Figure 4. (a) Optimized structures of **NaHB**; **(b)** FTIR spectra of **NaHB** at S_0 and S_1.

These factors favour the excited state intramolecular proton transfer phenomenon. Therefore, potential energy curves (PECs) were constructed with respect to proton transfer coordinate for **NaHB** enol form to keto form. According to the PECs, the enol form is the only stable conformer in the S_0 state and establish a relationship of **NaHB** (enol; 0 $kcalmol^{-1}$) < **NaHB** (keto; 3.37 $kcalmol^{-1}$) in S_0 state and **NaHB** (enol; 54.99 $kcalmol^{-1}$) > **NaHB** (keto; 50.24 $kcalmol^{-1}$) in the S_1 state **(Figure 5)**. Further, calculated energy barrier for forward proton transfer at S_0 state is 6.64 $kcalmol^{-1}$, which further decreases to 3.43 $kcalmol^{-1}$ at S_1 state. On the other hand, for reverse proton transfer has energy barrier of 3.37 $kcalmol^{-1}$ at S_0 state which increase to 8.18 $kcalmol^{-1}$ at S_1 state. These observations of low energy barrier for forward proton transfer and high barrier for backward proton transfer at S_1 state suggest the ESIPT process for **NaHB**.

View Article Online
DOI: 10.1039/D5NJ03370E

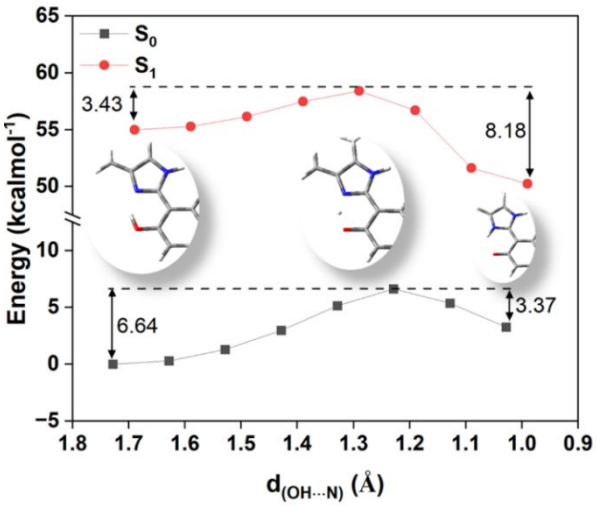

Figure 5. Energy profile of proton transfer for **NaHB** (truncated view of proton transfer is shown)

3.4 Sensing properties of NaHB towards various metals, anions and nerve agents

The absorption and emission behaviors of **NaHB** were investigated using CH_3CN: H_2O (9:1) medium. The **NaHB** exhibited absorption maxima (λ_{max}) at 402 nm, and an emission peak was observed at 520 nm in CH_3CN: H_2O (9:1) solvent media. The sensing behavior of **NaHB** has been explored towards various metal ions (Na^+, K^+, Mg^{2+}, Ba^{2+}, Al^{3+}, Ca^{2+}, Fe^{2+}, Fe^{3+}, Co^{2+}, Ni^{2+}, Cu^{2+}, Zn^{2+}, Ga^{3+}, Cd^{2+}, Hg^{2+} and Pb^{2+}), anions (CH_3COO^-, F^-, Cl^-, Br^-, CN^-, $H_2PO_4^-$, HSO_4^-, NO_3^-, AcO^-, ClO^-, $P_2O_7^{4-}$, SCN^-) and nerve agents (DCP, TEP (Triethyl phosphate), *N*-BP (*N*-Butyl phosphate)) using UV-Visible and fluorescence spectrophotometric techniques. We observed an exceptional response of **NaHB** towards Ga^{3+} ions and DCP and possessed high sensitivity and selectivity *via* an enhancement in the emission band whereas other anions and metal ions did not show any significant change in absorption and emission spectra.

3.4.1 UV-Vis spectral studies of NaHB towards Ga^{3+}

The UV-Vis spectral technique has been used for investigating the selective and sensitive ability of **NaHB** with various metal ions **(Figure S7(a))**. The UV–Visible absorption spectrum of the free probe **NaHB** displays two prominent absorption bands: a strong band at 402 nm and another at approximately 350 nm. The lower-wavelength band at 350 nm can be assigned to the π–π* transition within the aromatic naphthalimide–benzimidazole framework, while the more intense band at 402 nm is attributed to an intramolecular charge transfer (ICT) transition from the electron-donating imine and benzimidazole moieties to the electron-withdrawing naphthalimide unit. It was observed that the presence of Ga^{3+} ions in **NaHB** (10 μM) in

CH_3CN: H_2O (9:1) solvent revealed blueshift from 402 nm to 396 nm while all other metal ions did not show any significant response in the absorption spectrum. Upon incremental addition of Ga^{3+}, both absorption bands exhibit a distinct blue shift, the absorption intensity at 396 nm was increased and attained a plateau after the addition of 60 μM of Ga^{3+} ions **(Figure S7(b)),** indicating that complex formation perturbs the electronic structure of **NaHB**. The hypsochromic shift suggests a reduction in conjugation and suppression of ICT as a result of coordination between Ga^{3+} and the donor atoms (carbonyl oxygen and imine nitrogen) or interaction with the phosphoryl center of DCP. These interactions draw electron density away from the conjugated π-system, thereby increasing the HOMO–LUMO energy gap and shifting the absorption toward shorter wavelengths.

Notably, no observable color change occurred, confirming that the spectral shift remains confined to the UV region and does not extend into the visible range. Similar blue-shift behavior upon complexation has been previously reported for naphthalimide-based probes exhibiting ICT modulation upon metal ion binding.

3.4.2 Fluorescence spectral studies of NaHB towards Ga^{3+}

When excited **NaHB** (λ_{ex} = 402 nm, 10 μM, CH_3CN: H_2O (9:1)), a weak fluorescence intensity was observed at 520 nm. The addition of various metal ions to **NaHB** did not show any variation in the emission spectrum except Ga^{3+}. The presence of Ga^{3+} ions exhibited increase in fluorescence intensity with quick response at 520 nm, displaying excellent bright green fluorescence under UV light **(Figure 6(a))**.

Incremental addition of Ga^{3+} ions into the solution of **NaHB**, an emission enhancement was observed at the same wavelength of 520 nm **(Figure 6(b))**. The maximum emission intensity (8 times) was attained with the addition of 50 μM of Ga^{3+} ions. A good linear relationship of the fluorescence intensity was observed at the concentration range of 0-50 μM. The binding constant acquired from the titration data for Ga^{3+} ions, calculated from equation 2, was found to be **$5.15\times10^4 \pm 0.03 \times10^4$ M^{-1} (95% CI: $5.07 - 5.22 \times 10^4$ M^{-1})**. By using equation (1), the limit of detection (LOD) was found to be **36 ± 0.02 nM (95% CI: 35.95 – 36.05 nM)** and the quantifiable limit range was 36-120 nM in CH_3CN: H_2O (9:1). The obtained LOD value was compared with reported values for chemosensors, particularly naphthalimide-based derivatives using fluorometric methods, and was found to be superior to those previously reported **(Table S1)**. The fluorescence response of **NaHB** with Ga^{3+} and other metal ions can be seen under UV light by naked eye **(Figure 7).**

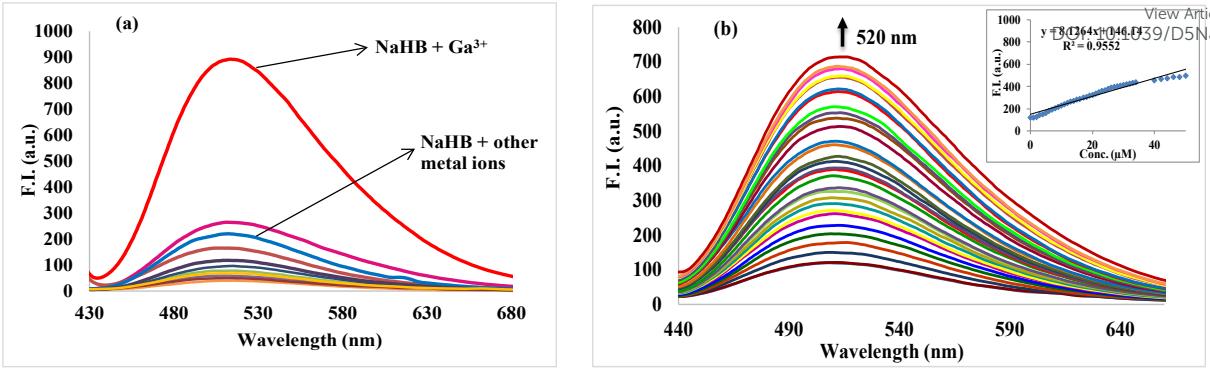

Figure 6. Fluorescence spectra of **NaHB** (10 μM) in CH_3CN: H_2O (9:1, [v/v]) **(a)** in presence of various metal ions (50 equiv.), and **(b)** on incremental addition of 0–50 μM of Ga^{3+} ions.

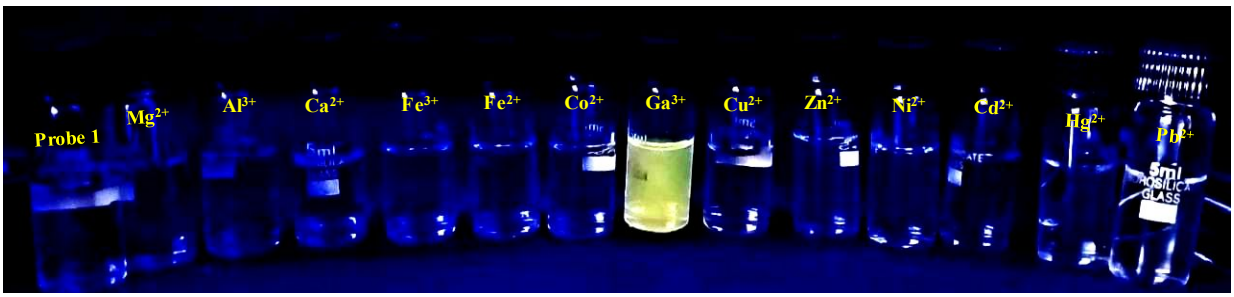

Figure 7. Effect of different metal ions on the solution of **NaHB** (10 μM, CH_3CN: H_2O (9:1, [v/v])) under UV light

3.4.3 Interference study

To demonstrate the fluorescence selectivity of **NaHB** towards Ga^{3+}, the interference study with some common intrusive ions (1 mM) has been examined. For the selective behavior of **NaHB** towards Ga^{3+} (50 μM), the interference studies were performed in CH_3CN: H_2O (9:1). By consecutive addition of different analytes (1 mM) in the complex of **NaHB** + Ga^{3+}, the spectral change has been measured. The study was done in 3 replicates and the standard deviations along with the p-value (probability of intereference of other analytes) obtained from t-test have been incorporated **(Table S2)**. The spectral signal does not get altered on the addition of other metal ions indicating no interference in the binding of **NaHB** + Ga^{3+}. This signifies that **NaHB** possesses no response-ability towards most of the analytes except Ga^{3+} ions **(Figure 8)**.

View Article Online
DOI: 10.1039/D5NJ03370E

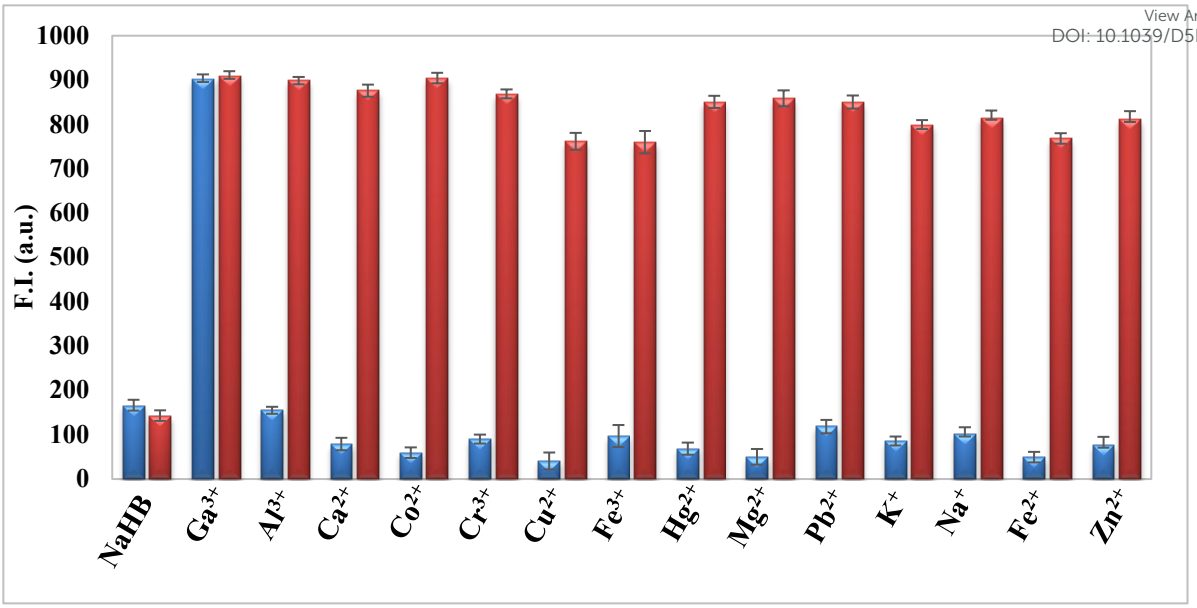

Figure 8. Blue bars represent the selectivity of **NaHB** (10 μM, CH_3CN: H_2O (9:1; v/v)), at λ_{em} = 520 nm upon the addition of different cations and red bars show the competitive selectivity of **NaHB** in the presence of Ga^{3+} ions

3.4.4 Binding behavior of NaHB towards Ga^{3+} ions

For determining the stoichiometry of complex of **NaHB** + Ga^{3+}, solutions of varying mole fractions of Ga^{3+} from 0.1 to 1.0 in CH_3CN: H_2O (9:1) were prepared. A graph was plotted within the emission response in each case at 520 nm and the mole fraction of Ga^{3+} ions **(Figure S8)**. Based on Job's plot, it was found that the ratio of complexation of Ga^{3+} ions and **NaHB** was 1:1. Moreover, the ratio of the formation of complex was confirmed by ESI-Mass spectral analysis. The mass was taken for the mixture of **NaHB** and Ga^{3+} in CH_3CN: H_2O (9:1) where a new peak at *m/z* = 546.4014 corresponds to the complex of (**NaHB** + Ga^{3+} - H^+) was observed **(Figure S9)**, supporting to formation of 1:1 complex.

3.4.5 UV-Vis spectral studies of NaHB towards various anions and nerve agents

UV-Visible spectra of **NaHB** were also recorded in the presence of various anions (1 mM) like CH_3COO^-, F^-, Cl^-, Br^-, I^-, CN^-, $H_2PO_4^-$, HSO_4^-, NO_3^-, AcO^-, ClO^-, $P_2O_7^{4-}$, SCN^- and nerve agents such as DCP (Diethyl chloro phosphate), TEP (Triethyl phosphate), *N*-BP (*N*-Butyl phosphate) in CH_3CN: H_2O (9:1). No significant change was observed in case of various analytes, while DCP showed a blue shift of 13 nm (at 389 nm) upon its addition to **NaHB (Figure 9(a))**. The interaction of the probe with DCP was systematically examined by UV–Vis titration studies in CH_3CN: H_2O (9:1) **(Figure 9(b))**. Upon incremental addition of DCP to the solution of the probe, the absorption spectra exhibited significant changes, indicating strong host–guest

View Article Online
DOI: 10.1039/D5NJ03370E

interaction. A gradual increase (hyperchromic effect) in the absorption band at 389 nM was observed, accompanied by a slight hypsochromic shift. A plateau was obtained after the addition of 50 μM of DCP during titration, suggesting effective binding of DCP at the recognition site of the probe.

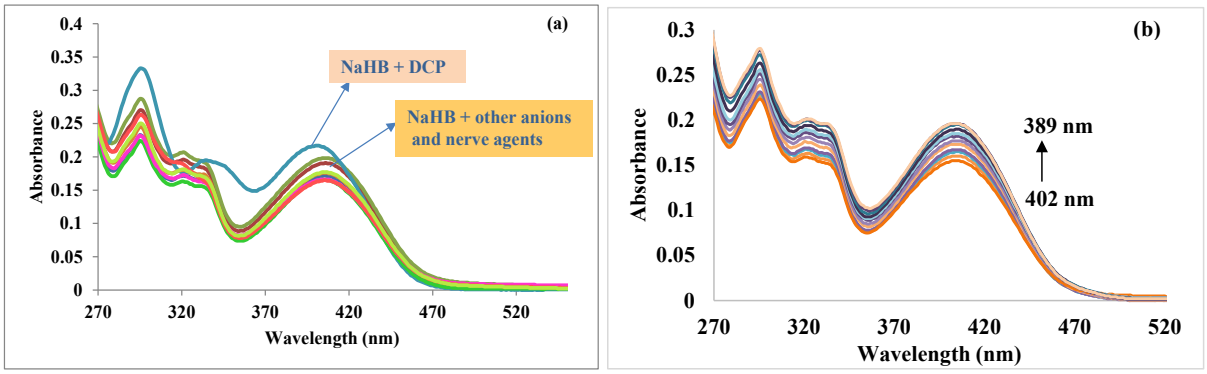

Figure 9. (a) UV-visible spectra of **NaHB** (10 μM, CH_3CN: H_2O (9:1)) in the presence of various anions (50 equiv.) and **(b)** on incremental addition of DCP (0-50 μM)

3.4.6 Fluorescence spectral studies of NaHB towards anions

To check the selectivity and sensitivity of **NaHB** towards DCP, fluorescence response was also studied. It was found that while complexing of DCP with **NaHB**, the fluorescence intensity showed a remarkable 7 folds enhancement at 515 nm. No other anion or nerve agent has shown any change in the emission spectrum **(Figure 10(a))**. Fluorescence titrations were carried out with 10 μM of **NaHB** along with varying concentrations of DCP **(Figure 10(b))**. A linear relation of increase in fluorescence intensity with increasing concentration of DCP in **NaHB** was noticed. This linear graph was used to obtain the K_a (binding constant) value using the Benesi-Hildebrand equation and was found to be **1.2 x 10^5 M^{-1} (95% CI: 1.10 – 1.29 × 10^5 M^{-1})**. The limit of detection (LOD) obtained for DCP was **11 nM (95% CI: 10.92 – 11.07 nM)** and the quantifiable limit was 11-37 nM. A competitive complexation study was carried out to view the possible invasion of some other analyte in the complex **NaHB** + DCP. The bar graph shows the variation in fluorescence intensity of complex in the presence of different anions and nerve agents **(Figure S10(a))**. It can be inferred from the graph that no other ion interfered in the complex of **NaHB** + DCP, signifying selectivity for DCP only. To depict the stoichiometry, Job's plot studies were done and it was observed to be 1:1, which can be seen from the graph **(Figure S10(b))**. To further support Job's plot, ESI-Mass spectrum of **NaHB** in the presence of DCP was obtained. A reaction was performed between **NaHB** and DCP to isolate and determine the mass of the product formed. The HRMS (ESI+) of the isolated

View Article Online
DOI: 10.1039/D5NJ03370E

reaction material showed a prominent ion at $m/z \approx [M + 136 + H]^+$ (m/z = 615.1794, calcd. 615.1790, Δ = 8 ppm), indicating addition of a mass equivalent to DCP (≈ +136 Da) **(Figure S11(a))**. However, tandem MS (MS/MS) of this ion under collision-induced dissociation conditions reproducibly produced the parent probe ion (m/z = 479.1509) and free DCP fragments (m/z = 137) as the major products **(Figure S11(b))**, even at moderate collision energies, indicating facile cleavage of the added mass. This fragmentation behavior strongly suggests that the interaction between **NaHB** and DCP is primarily non-covalent.

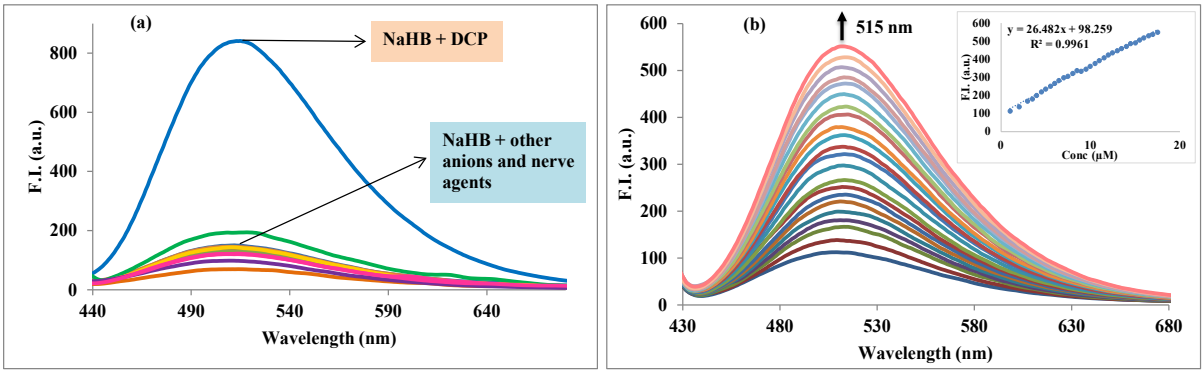

Figure 10. **(a)** Fluorescence spectra of **NaHB** (10 μM) in CH_3CN: H_2O (9:1, [v/v]) in the presence of various anions and nerve agents (1 mM) and **(b)** on incremental addition of DCP ions (0–25 μM)

3.5 NMR titrations and binding mechanism

^{1}H NMR titrations were performed in CD_3CN to investigate the binding mechanism of **NaHB** with Ga^{3+} and DCP. Upon addition of 1 equiv. of Ga^{3+} ions to **NaHB**, the protons H_a and H_b at 6.67-6.72 ppm and protons H_c and H_d at 7.02-7.06 ppm got shifted downfield to 6.78-6.86 ppm ($H_{a'}$ and $H_{b'}$) and 7.14-7.20 ppm ($H_{c'}$ and $H_{d'}$), respectively. Moreover, $H_{e'}$ proton gets slightly deshielded from 7.76-7.78 ppm to 7.78-7.81 ppm **(Figure 11)**. A similar trend was seen in case of DCP binding with **NaHB**. The $H_{a''}$ and $H_{b''}$ protons experienced deshielding with a shift of 0.13-0.16 ppm during the complexation of DCP with **NaHB**. Similarly, Hc'' and Hd'' protons also shifted towards the downfield region (7.15-7.20 ppm). However, the $H_{e''}$ and $H_{f''}$ protons have not experienced the shifts as these protons were far from the binding sites, but a doublet from **NaHB** of H_e gets almost detached from the multiplet, thereby increasing the range from 7.76-7.78 ppm to 7.76-7.81 ppm. The results indicated that in case of complexation with Ga^{3+}, both imine nitrogen and hydroxyl group were involved, making the nearby protons de-shielded. The deprotonation of the hydroxyl group was caused by the phosphate group of DCP, therefore shifting the proton signals to the downfield region. Moreover, no further change was observed

View Article Online
DOI: 10.1039/D5NJ03370E

with increasing equiv. of the analyte confirming the stoichiometry as 1:1, as obtained from Job's plot.

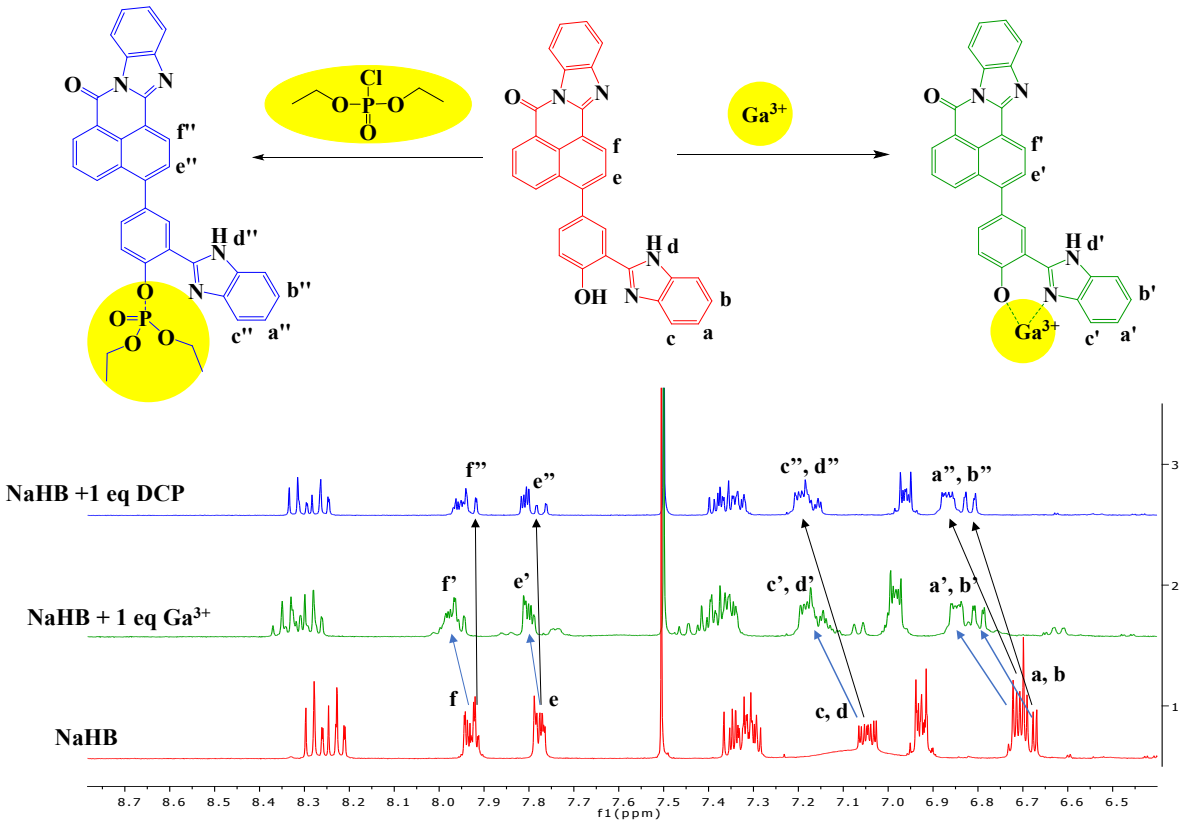

Figure 11. ^{1}H NMR spectra of **NaHB** (5 mM) in the absence and presence of Ga^{3+} ions and DCP in CD_3CN (d_3) (1 equiv.)

In order to further confirm the binding behaviour of **NaHB** towards Ga^{3+} ions, theoretical calculations have also been performed. **NaHB**.Ga^{3+} was optimized at S_0 state and correspondingly vertical-excitations were calculated **(Figure 12)**. It has been noted that **NaHB**.Ga^{3+} have $S_0 \rightarrow S_1$, $S_0 \rightarrow S_2$ and $S_0 \rightarrow S_3$ excitations at 520 nm (HOMO→LUMO (98 %); f = 0.0001), 430 nm (HOMO→LUMO+1 (97.4 %); f = 0.5994) and 424 nm (HOMO-2→LUMO (98 %); f = 0.0001), respectively. Further, only $S_0 \rightarrow S_2$ was analysed, as it contributes as bright excitation and it showed electron density shifts towards naphthalimide unit with electron-hole overlap (Sr = 0.71310) and charge separation of 1.715 Å. Further, it can be noted that the electron-hole overlap for **NaHB**.Ga^{3+} increased relative to **NaHB**.DCP and **NaHB**, while the electron-hole centroid distance decreased, which signifies that the quantity of intramolecular charge transfer decreases for **NaHB**.Ga^{3+}.

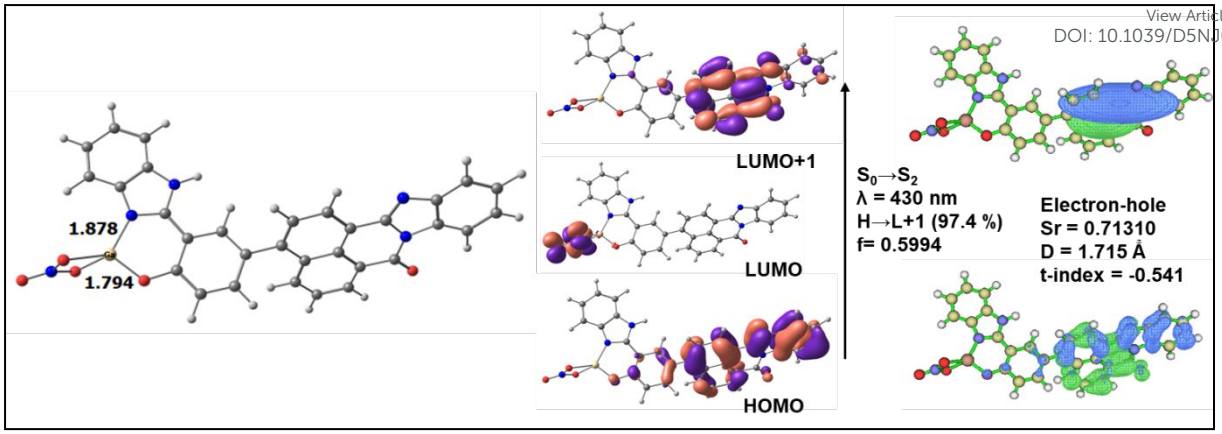

Figure 12. Optimized structure and frontier molecular orbitals of **NaHB** with Ga^{3+} (stoichiometry 1:1) and the electron-hole distribution of S_0-S_2 orbitals

Additionally, we investigated the interaction between DCP and **NaHB**, where **NaHB**.DCP complex was formed **(Figure 13)**. Furthermore, we examined the vertical Frank-Condon excitation to have an insight into the absorption spectra of the complex. It was noted that **NaHB**.DCP has $S_0 \rightarrow S_1$ excitation at 432 nm with an oscillation strength of 0.5025 from 98.4% contribution of HOMO→LUMO transition. The preceding $S_0 \rightarrow S_2$ and $S_0 \rightarrow S_3$ transition were calculated at 411 nm (HOMO-1→LUMO (98%); f = 0.02660), and 370 nm (HOMO-3→LUMO (94 %); f = 0.03070), respectively. Further, the HOMO→LUMO transition has the nature of intramolecular charge transfer that shows the electron density shifts from benzimidazole and connecting phenyl unit to naphthalimide unit with low electron-hole overlap (Sr = 0.60635) and charge separation of 4.1 Å.

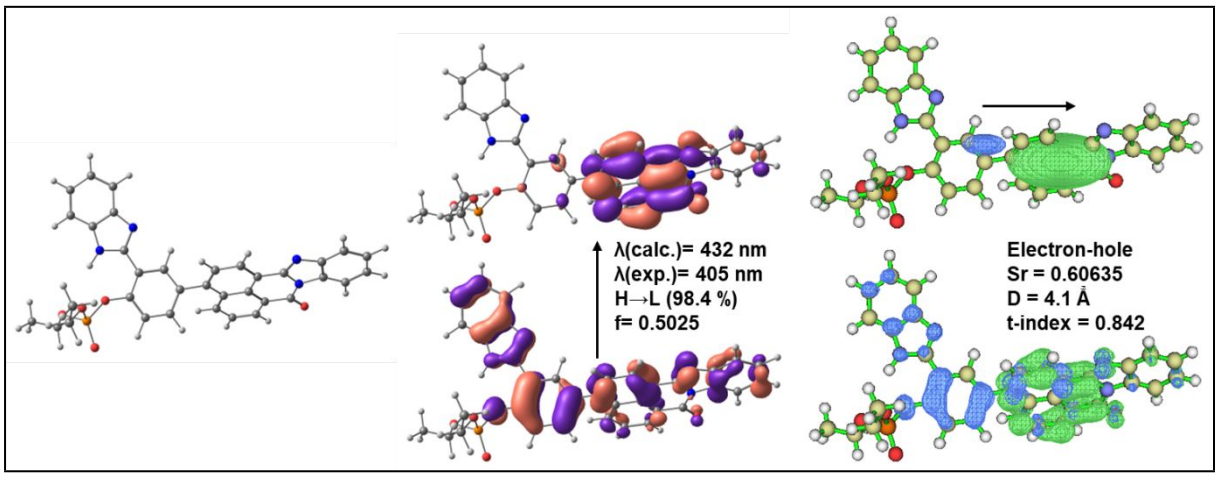

Figure 13. Optimized structure and frontier molecular orbitals of **NaHB** with DCP (stoichiometry 1:1) and the electron-hole distribution of S_0-S_1 orbitals

3.6 Lifetime measurements

Life-time decay studies were also done for both probe **NaHB** and its complexes with Ga^{3+} and DCP. Upon complexation of **NaHB** with Ga^{3+} (1 equiv.) and DCP (1 equiv.), a significant change was observed in the decay profiles in both cases (**Figure 14)**. The average lifetime value (τ_{av}) of **NaHB** was calculated using three-exponential fitting and was found to be 0.177 ns **(eq. 3)**.

$$\tau_{avg} = \frac{\sum \alpha_i \tau_i^2}{\sum \alpha_i \tau_i} \quad \text{..... (3)}$$

where $\alpha_i = \alpha_1$, α_2 and α_3 are the normalized pre-exponential factors, and $\tau_i = \tau_1$, τ_2 and τ_3 represent the excited-state lifetimes of the corresponding components. On complexation with Ga^{3+}, the lifetime changed to 0.286 ns and with DCP, the value obtained was 0.231 ns **(Table 2)**. Thus, on complexation, the average excited lifetime of **NaHB** was found to be increased, and the ESIPT from the hydroxyl group of **NaHB** was fully inhibited, hence, in consequence, the fluorescence intensity was enhanced on binding of **NaHB** with Ga^{3+} and DCP.

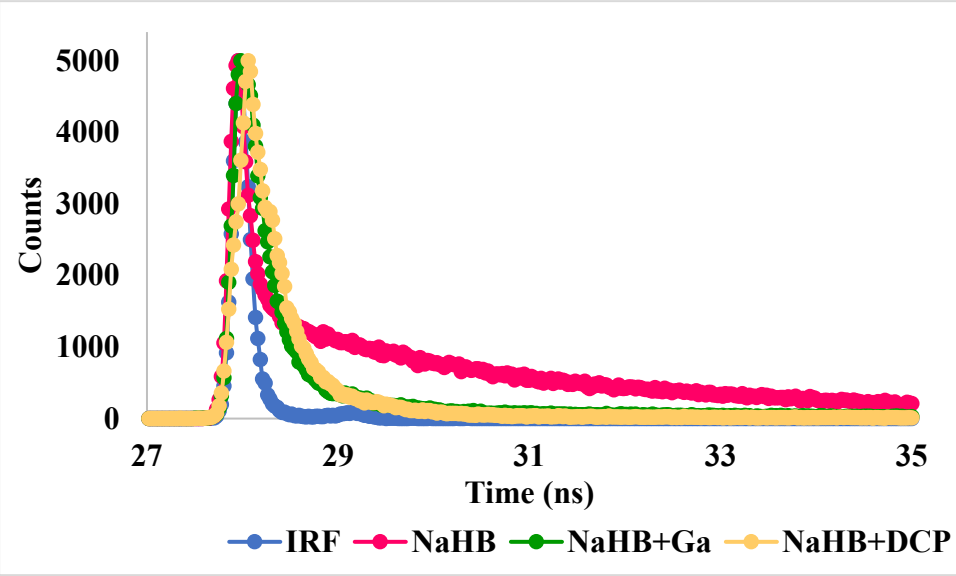

Figure 14. Fluorescence lifetime decay of **NaHB** along with Ga^{3+} and DCP

Table 2. Fluorescence lifetime decay profile

	τ_1 (ns)	τ_2 (ns)	τ_3 (ns)	α_1	α_2	α_3	χ^2	τ_{av} (ns)
NaHB	1.45	4.92	0.04	0.02	0.02	0.96	1.06	0.177
NaHB + Ga^{3+}	0.69	0.22	3.91	0.04	0.95	0.01	1.07	0.286
NaHB + DCP	0.41	0.11	3.33	0.30	0.69	0.01	1.11	0.231

View Article Online
DOI: 10.1039/D5NJ03370E

3.7 Reversible Studies

Another desirable property for the development of chemosensor for its application in real world is the reversibility. The experiment has been performed by sequential addition of Ga^{3+} (1 equiv.) and EDTA (1 equiv.) in **NaHB** by measuring the fluorescence intensity. When 1 equiv. of Ga^{3+} was added to **NaHB**, the fluorescence gets enhanced to 8 folds, while on addition of EDTA (1 equiv.), the fluorescence intensity gets quenched. This is because of the de-complexation of **NaHB** + Ga^{3+} complex as EDTA form complex with Ga^{3+} because of its strong affinity for metal ions, making **NaHB** free. The fluorescence was regained in the system of **NaHB** + Ga^{3+} + EDTA by adding another 1 equiv. of Ga^{3+}. Hence, the addition of Ga^{3+} and EDTA alternatively would result in on-off-on cycles. The cycle was repeated 5 times, signifying a good reusability of **NaHB** towards Ga^{3+} **(Figure 15)**.

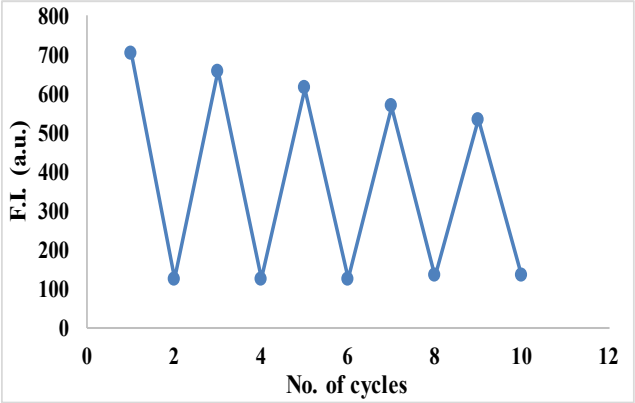

Figure 15. The reversible and reproducible emission signal at 520 nm (λ_{ex} = 402 nm, 10 μM) in CH_3CN: H_2O (9:1, [v/v]) on repetitive addition of metal ions and EDTA.

3.8 Practical application

3.8.1 Paper-strip based sensing of Ga^{3+} and DCP

Costly instrumental techniques and extensive experimental procedures are the major drawbacks to the practical usage of chemosensors. In this view, paper strips are gaining much interest in the sensing area because of their portability and cost-effectiveness. For on-site detection of Ga^{3+} and DCP using **NaHB**, Whatman-41 filter paper-based strips were prepared by immersing them into the solution of **NaHB** (10^{-3} M) in CH_3CN: H_2O (9:1) for 5 minutes and then air-dried for several hours. Subsequently, aqueous solutions of Ga^{3+}at different concentrations ranging from 10^{-1} M to 10^{-6} M were added dropwise onto the coated strips. The interaction between Ga^{3+} ions and the NaHB on the strips was monitored visually, with particular attention to any observable changes such as color variation or intensity, which could

View Article Online
DOI: 10.1039/D5NJ03370E

indicate complex formation or sensor response **(Figure S12)**. Following this, different ion solutions (10^{-1} M) were added dropwise to the strips and then allowed to spread on the surface of the prepared coated strips in air. The fluorescence intensity of the paper strip consisting of Ga^{3+} and DCP was quite high when observed under 365 nm UV lamp **(Figure 16)**. This implies that the fabricated paper strips of **NaHB** can be used for on-spot detection of Ga^{3+} and DCP in the presence of other metal ions, anions and nerve agents.

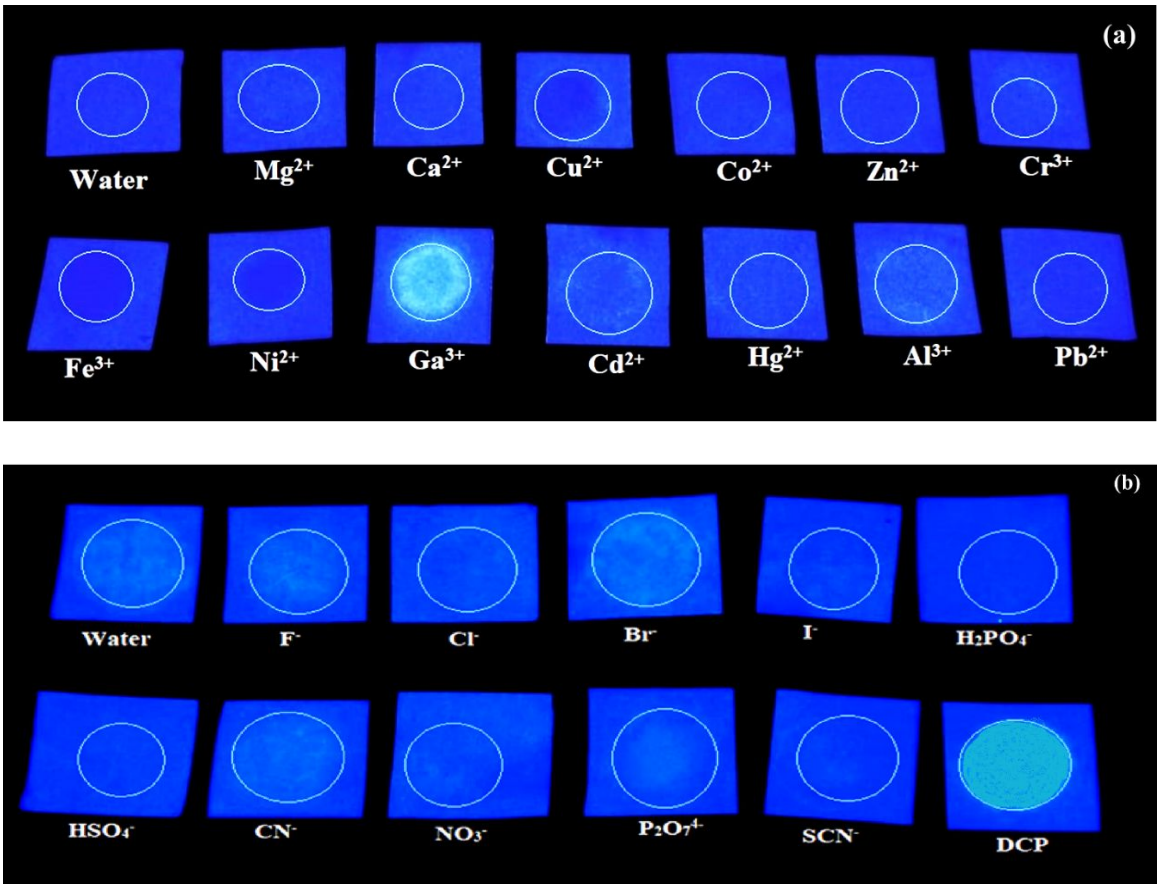

Figure 16. Paper strips coated with **NaHB** along with **(a)** dropwise addition of different metal ions (10^{-2} M) and **(b)** dropwise addition of different anions (10^{-1} M)

3.8.2 Real-time monitoring in water samples

The application of chemosensors should not be limited to lab-used chemicals only, it should also be used for monitoring of analytes in real environmental samples. To evaluate the practical applicability and accuracy of the developed probe **NaHB**, a calibration curve was constructed using real water samples (tap, sewage, and Ghaggar river water) spiked with known concentrations of Ga^{3+} and DCP ions. The corresponding ion concentrations were then interpolated from the calibration curve using the measured fluorescence intensities. The

fluorescence spectra of each spiked sample were recorded under identical conditions to those used in standard solution studies **(Figure 17)**.

A gradual enhancement in fluorescence intensity was observed with increasing analytes concentration, confirming that the sensor responds reliably in complex water matrices. The calibration curve, plotted as fluorescence intensity versus ion concentration, exhibited a good linear relationship within the tested range, following the regression equation 4:

$$I = mC + b \qquad \text{(4)}$$

where I represent the measured fluorescence intensity, C is the Ga^{3+} concentration, m is the slope (sensitivity), and b is the intercept.

The high correlation coefficient ($R^2 \approx 0.99$) demonstrates excellent linearity and reproducibility of the response. The close agreement between the measured and spiked concentrations, as reflected in satisfactory recovery values **(Table 3)** (typically 98–102%), further confirms that the probe maintains its fluorescence enhancement behavior and quantitative detection, capability for Ga^{3+} and DCP even in real environmental water samples.

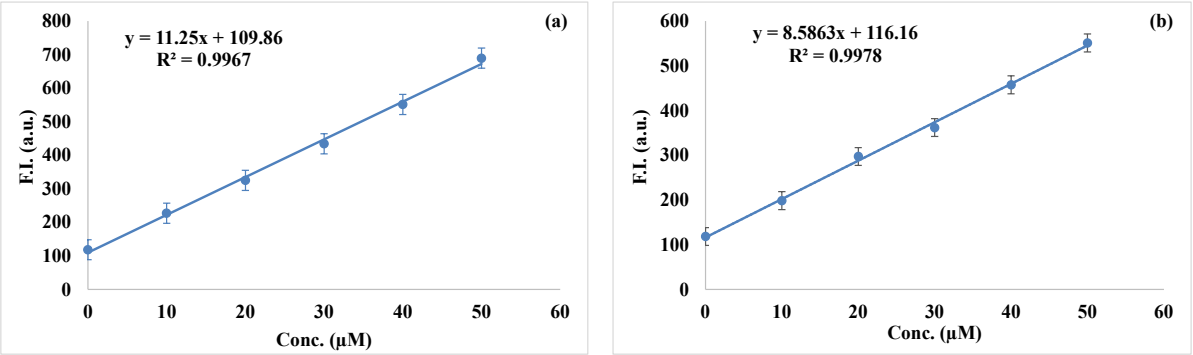

Figure 17. Fluorescence spectra of **NaHB** in different concentrations of spiked (a) Ga^{3+} and (b) DCP from 0 to 50 µM

Table 3. Analyzing Ga^{3+} and DCP quantitatively in real water samples

	Ga^{3+} (μ M)	Found (μ M)	RSD (%)	Recovery (%)		DCP (μ M)	Found (μ M)	RSD (%)	Recovery (%)
Tap water	10	9.8	1.15	98.7	Tap water	10	9.9	0.59	99.3
	20	19.9	0.33	99.7		20	19.9	0.52	101.5
	30	29.7	1.06	99.1		30	29.9	1.07	99.8
Sewage water	10	9.9	0.71	99.3	Sewage water	10	9.8	0.95	98.9
	20	20.2	2.84	101.1		20	19.6	2.84	98
	30	29.8	2.65	99.4		30	29.7	0.7	99.3
Ghaggar river water	10	10.1	3.31	101.3	Ghaggar river water	10	10.1	3.09	101.4
	20	19.8	0.63	99.4		20	19.9	0.2	99.9
	30	29.8	0.91	99.3		30	30.4	1.83	101.4

View Article Online
DOI: 10.1039/D5NJ03370E

3.8.3 Molecular logic gate

The molecular logic gate was fabricated with **NaHB**, Ga^{3+} and EDTA. The emission band at 520 nm appears due to the formation of complex of **NaHB** and Ga^{3+} ions. When EDTA was added to the complex, the emission intensity at 520 nm was highly quenched. In this view, an 'INHIBIT' logic gate is made by taking Ga^{3+} and EDTA as chemical inputs and the emission intensity at 520 nm as output. The inhibition is caused possibly by the de-complexation of **NaHB** + Ga^{3+} complex and Ga^{3+} getting attached to EDTA, thereby giving no enhanced emission signal because of the strong binding characteristics of EDTA as ligand. By de-complexation, the optical properties of the probe were reversed. The molecular logic gate and the truth table are shown in (**Figure 18)**. It can be inferred from the truth table that the output comes out to be '**1**' only when the **NaHB** + Ga^{3+} complex is formed. Once EDTA enters the solution, the output comes out to be '**0**' in all other cases.

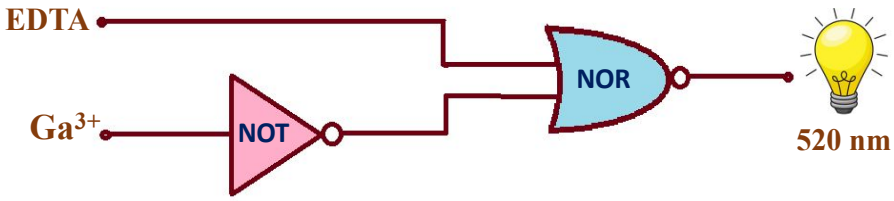

Input		Output
IN1 = Ga^{3+}	IN2 = EDTA	**OUT = λ_{520} nm**
0	0	0
0	1	0
1	0	1
1	1	0

Figure 18. Logic gate and Truth table

Conclusion

The fluorescence-based probe **NaHB** effectively enabled the selective and sensitive detection of $Ga^{3+}$and DCP, with significant emission enhancement upon analyte binding which is clearly visible under UV light. This fluorescence response allowed for nanomolar-level detection limits of 36 nM for Ga^{3+} and 11 nM for DCP. The underlying binding mechanisms were further supported and confirmed by detailed NMR spectroscopy, mass spectrometry, and computational studies. The interaction of Ga^{3+} with both the hydroxyl and imine groups of **NaHB** led to a stable six-membered chelate ring, while DCP selectively engaged the hydroxyl

site. Additionally, paper strip-based sensing under UV light enabled practical, on-site application, and the probe **NAHB** performed reliably in real water samples including tap, drinking, and river water. The **NaHB**–Ga^{3+}complex also demonstrated logic gate functionality using $Ga^{3+}$and EDTA as inputs, expanding the potential for molecular computation.

Conflicts of interest

There are no conflicts of interest to declare.

Acknowledgements

VL thanks CEEMS (Project No. TIET/CEEMS/Regular/2023/8054), VT-India, for providing funds. SAI Labs, TIET, Patiala and SAIF, PU, Chandigarh, for NMR. ACALAB and TIET for NMR and DST-FIST (SR/FST/CS-II/2018/69) for HRMS analysis are also acknowledged.

References

1. A. Mumthaj and M. Umadevi, *Spectrochim. Acta - Part A Mol. Biomol. Spectrosc.*, 2024, **308**, 123741-123747.
2. B. Devi, A. K. Guha and A. Devi, *Spectrochim. Acta - Part A Mol. Biomol. Spectrosc.*, 2024, **305**, 123448-123453.
3. N. A. Bumagina, A. A. Ksenofontov, E. V. Antina and M. B. Berezin, *Spectrochim. Acta - Part A Mol. Biomol. Spectrosc.*, 2024, **307**, 123663-123675.
4. X. Gao, X. Wang, W. Lv, N. Wang, M. Yang and Q. Zhang, *J. Mol. Struct.*, 2022, **1250**, 131792-131800.
5. J. Singh, B. Mohan, A. Kumar, P. Bhardwaj and R. K. Chauhan, *J. Fluoresc.*, 2024, **34**, 149–157.
6. K. Zhang, X. Tian, P. Xu, Y. Zhu, S. Guang and H. Xu, *Spectrochim. Acta - Part A Mol. Biomol. Spectrosc.*, 2024, **318**, 124484-124493.
7. F. Sun, L. Yang, S. Li, Y. Wang, L. Wang, P. Li, F. Ye and Y. Fu, *J. Agric. Food Chem.*, 2021, **69**, 12661–12673.
8. D. Yun, J. M. Jung and C. Kim, *Inorganica Chim. Acta*, 2018, **479**, 154–160.
9. J. W. van Dam, M. A. Trenfield, C. Streten, A. J. Harford, D. Parry and R. A. van Dam, *Ecotoxicol. Environ. Saf.*, 2018, **165**, 349–356.
10. H. Xiang, T. Wang, S. Tang, Y. Wang and N. Xiao, *Spectrochim. Acta - Part A Mol. Biomol. Spectrosc.*, 2022, **267**, 120510-120519.
11. J. M. Kikkawa and D. D. Awschalom, *Nature*, 1999, **397**, 139–141.

12. H. M. Kim, Y. H. Cho, H. Lee, S. I. I. Kim, S. R. Ryu, D. Y. Kim, T. W. Kang and K. S. Chung, *Nano Lett.*, 2004, **4**, 1059–1062.
13. R. Trotta, P. Atkinson, J. D. Plumhof, E. Zallo, R. O. Rezaev, S. Kumar, S. Baunack, J. R. Schröter, A. Rastelli and O. G. Schmidt, *Adv. Mater.*, 2012, **24**, 2668–2672.
14. J. Yoon, S. Jo, I. S. Chun, I. Jung, H. S. Kim, M. Meitl, E. Menard, X. Li, J. J. Coleman, U. Paik and J. A. Rogers, *Nature*, 2010, **465**, 329–333.
15. S. L. Yao, R. H. Wu, P. Wen, H. Liu, T. Tu and S. J. Liu, *J. Mol. Struct.*, 2024, **1297**, 136925-136931.
16. S. J. O. White and J. P. Shine, *Curr. Environ. Heal. reports*, 2016, **3**, 459–467.
17. A. Tanaka, *Toxicol. Appl. Pharmacol.*, 2004, **198**, 405–411.
18. L. Ann Burns and R. T. Abraham, *Cancer Res.*, 1993, **53**, 1862–1866.
19. J. Qi, Q. Yao, K. Qian, L. Tian, Z. Cheng, D. Yang and Y. Wang, *Eur. J. Med. Chem.*, 2018, **154**, 91–100.
20. Y. Zhang and B. Li, *J. Mol. Struct.*, 2022, **1250**, 131461-131467.
21. S. Zhang, B. Yang, B. Yuan, C. Zhou, M. Zhang, Y. Zhao, P. Ye, L. Li and H. Li, *ACS Sensors*, 2023, **8**, 1220–1229.
22. Y. J. Jang, K. Kim, O. G. Tsay, D. A. Atwood and D. G. Churchill, *Chem. Rev.*, 2015, **115**, 1–76.
23. M. S. J. Khan, Y. W. Wang, M. O. Senge and Y. Peng, *J. Hazard. Mater.*, 2018, **342**, 10–19.
24. E. D. Fussell, N. D. Kline, E. Bennin, S. S. Hirschbeck and A. Darko, *ACS Sensors*, 2024, **9**, 2325–2333.
25. S. Costanzi, J. H. Machado and M. Mitchell, *ACS Chem. Neurosci.*, 2018, **9**, 873–885.
26. S. Banerjee, P. Ghosh, A. Karak, D. Banik and A. K. Mahapatra, *Anal. Methods*, 2025, **17**, 432-439.
27. P. Zheng, A. Abdurahman, G. Liu, H. Liu, Y. Zhang and M. Zhang, *Sensors Actuators, B Chem.*, 2020, **322**, 128611-128618.
28. Z. Qiu, Y. Xiao, L. Zhang, Y. Miao, B. Zhang, X. Zhu, L. Ding, H. Peng and Y. Fang, *Chem. Commun.*, 2024, **60**, 9773–9776.
29. Q. Chen, Y. Sun, S. Liu, J. Zhang, C. Zhang, H. Jiang, X. Han, L. He, S. Wang and K. Zhang, *Sensors Actuators, B Chem.*, 2021, **344**, 130278-130300.
30. T. Qin, Y. Huang, K. Zhu, J. Wang, C. Pan, B. Liu and L. Wang, *Anal. Chim. Acta*, 2019, **1076**, 125–130.
31. Y. Yang, H. F. Ji and T. Thundat, *J. Am. Chem. Soc.*, 2003, **125**, 1124–1125.

32. R. Subramaniam, C. Åstot, L. Juhlin, C. Nilsson and A. Östin, *Anal. Chem.*, 2010, **82**, 7452–7459.
33. K. A. Joshi, M. Prouza, M. Kum, J. Wang, J. Tang, R. Haddon, W. Chen and A. Mulchandani, *Anal. Chem.*, 2006, **78**, 331–336.
34. G. Paimard, M. Nejatian, Z. Sarlak, R. Mohammadi and M. Rouhi, *Microchem. J.*, 2024, **198**, 110173-110198.
35. M. Verma, V. Luxami and K. Paul, *Eur. J. Med. Chem.*, 2013, **68**, 352–360.
36. T. Mishra, S. Guria, J. Sadhukhan, D. Das and M. Kumar, *J. Photochem. Photobiol. A Chem.*, 2024, **446**, 115168-115180.
37. P. M. W. Gill, B. G. Johnson, J. A. Pople and M. J. Frisch, *Chem. Phys. Lett.*, 1992, **197**, 499–505.
38. B. Das, M. Dolai, A. Dhara, A. Ghosh, S. Mabhai, A. Misra, S. Dey and A. Jana, *J. Phys. Chem. A*, 2021, **125**, 1490–1504.
39. Tian Lu, Feiwu Chen, Multiwfn: A Multifunctional Wavefunction Analyzer, *J. Comput. Chem.*, 2012, **33**, 580-592
40. Tian Lu, A comprehensive electron wavefunction analysis toolbox for chemists, Multiwfn, *J. Chem. Phys.*, 2024, **161**, 082503
41. G. Kumar, K. Paul, and V. Luxami, *New J. Chem.*, 2020, **44**, 12866-12874.

View Article Online
DOI: 10.1039/D5NJ03370E

Data Availability Statement

Data shall be available on request.